Chapter 7

N_2 Dissociation on W(110): an *Ab Initio* Molecular Dynamics Study on the Effect of Phonons

This chapter is based on:

F. Nattino, F. Costanzo and G. J. Kroes, J. Chem. Phys. **142**, 104702 (2015).

Abstract

Accurately modeling the chemisorption dynamics of N_2 on metal surfaces is of both practical and fundamental interest. The factors that may have hampered this achievement so far are the lack of an accurate density functional and the use of approximate methods to deal with surface phonons and non-adiabatic effects. In the current work, the dissociation of molecular nitrogen on W(110) has been studied using *ab initio* molecular dynamics (AIMD) calculations, simulating both surface temperature effects, such as lattice distortion, and surface motion effects, like recoil. The forces were calculated using density functional theory, and two density functionals were tested, namely the PBE and the RPBE functionals. The computed dissociation probability considerably differs from earlier static surface results, with AIMD predicting a much larger contribution of the

indirect reaction channel, in which molecules dissociate after being temporally trapped in the proximity of the surface. Calculations suggest that the surface motion effects play a role here, since the energy transfer to the lattice does not allow molecules that have been trapped into potential wells close to the surface to find their way back to the gas phase. In comparison to experimental data, AIMD results overestimate the dissociation probability at the lowest energies investigated, where trapping dominates, suggesting a failure of both tested exchange-correlation functionals in describing the potential energy surface in the area sampled by trapped molecules.

7.1 Introduction

Heterogeneous catalysis is employed in various industrial processes, of which ammonia synthesis is probably the most famous example. This industrial procedure, also known as the Haber-Bosch process, is based on the reaction of nitrogen and hydrogen over an iron catalyst. The dissociative chemisorption of N_2 on the catalyst is believed to be the rate-limiting step of the full process [1] and for this reason the reactive and non-reactive scattering of molecular nitrogen from metal surfaces has been the subject of many studies, with the aim of promoting a fundamental understanding on the key-elements that play a role in this reaction.

Tungsten surfaces, among others, have received much attention [2–21], with particular focus on the large crystallographic anisotropy that this metal exhibits with respect to nitrogen adsorption. For instance, the thermal reactivity of W(100) is about two orders of magnitude larger than the W(110) reactivity [2]. Molecular beam experiments found typical non-activated behaviour for the dissociation of N_2/W(100), with a non-zero sticking probability S_0 at vanishing incidence energies, and S_0 first decreasing, then increasing with increasing collision energy [9]. On the other hand, a monotonically increasing sticking probability function was observed for N_2/W(110), suggesting that only activated paths might lead to dissociation on this surface [5]. Alducin et al. [12–14] were able to show that this apparently activated behaviour could be reproduced by calculations performed on a potential energy surface (PES) that includes non-activated paths

for dissociation. However, the 'shape' of the PES is such that these non-activated paths are difficult to access at low collision energies.

The PES first used by Alducin et al. [12,13] for N_2/W(110), which includes all the six molecular degrees of freedom, was calculated with DFT at the generalized gradient approximation (GGA) level, using the PW91 exchange-correlation functional [22, 23]. The agreement with experiments, however, was not quantitative: The sticking probability curve at normal incidence angle exhibits a 'bump' between 0 and 500 meV, which was not observed in the experiments. The bump is caused by the dissociation of molecules that are temporally trapped in the proximity of the surface, due to the energy transfer from the molecules' normal translational component to other molecular degrees of freedom (dynamic trapping). A different PES, which was computed with a different GGA density functional, the RPBE functional [24], produced better agreement for normal incidence, but dramatically failed at describing the reactivity at 60° incidence angle [15], with the majority of the molecules being scattered at large distance from the surface (about 3 Å). The authors concluded that the PW91-PES is less accurate close to the surface, in the area where the dissociation takes place, while the RPBE-PES is too repulsive at larger distances from the surface. A similar conclusion concerning the RPBE-PES was obtained from a comparison of non-reactive scattering simulations to experiments, which also suggested that the PW91-PES is too corrugated [19].

Modeling non-adiabatic effects for N_2/W(110), such as electron-hole pair excitation, was first tackled by Juaristi et al. [16]. The energy transfer from molecular to electronic degrees of freedom was modeled as energy dissipation, included in the dynamics through friction coefficients. Such coefficients were calculated using the local density friction approximation (LDFA), and the electronically non-adiabatic results deviated only slightly from the fully adiabatic calculations [16, 18]. However, discussion is still open about the appropriateness of the LDFA for computing friction coefficient [25–28].

Martin-Gondre et al. [20] simulated the rotationally inelastic scattering of N_2 from W(110) simultaneously modeling energy dissipation to phonons, using the approximate generalized Langevin oscillator (GLO) model, and taking into account non-adiabatic

effects, using the LDFA. They found that the inclusion of phonon dissipative forces is more relevant than electronic ones, and suggested that the static surface electronically adiabatic calculations already include relevant aspects of the scattering dynamics. More recently, Petuya et al. looked at the non-reactive scattering of N_2 from W(100) [21]. They modeled energy dissipation to phonons using the GLO method, and compared these results to static-surface data and to experiments, finding reasonable agreement between experimental data and both models.

In a very recent study [29], the dissociation of N_2 on W(110) has been investigated using density functionals in which the correlation has been corrected to account for dispersion interactions [30, 31]. The authors have shown that some of these density functionals better describe properties such as adsorption energy and barriers for dissociation and desorption from the adsorption configuration that they have determined. Furthermore, the long range attractive interaction can correct for the excessive repulsion generated by some functionals (e.g. RPBE) at large distances from the surface, and also lower the barrier for dissociation most sampled by the molecules dissociating at 60° incidence angle. However, despite all the improvements achieved in the static properties of the PES, none of the tested vdW-corrected functionals has been found able to provide an overall good agreement with experimental data both at normal incidence and at a 60° incidence angle within the static surface approximation.

Summarizing, modeling both the reactive and the non-reactive scattering of N_2 from tungsten surfaces remains a challenge, and it is not clear whether the main cause of errors is the lack of an accurate exchange-correlation functional, or the use of approximate models to deal with surface temperature and surface motion effects and electronic non-adiabaticity in the dynamics. For this type of system, calculations explicitly including surface atom motion are desirable. In the first place, they could serve as a benchmark for models that aim at approximately describing the effect of surface phonons. Furthermore, if DFT-AIMD calculations employing a specific density functional could demonstrate good agreement with experiments on both reactive and non-reactive scattering, this would suggest that electron-hole pair excitation affects the dynamics only

marginally [28]. On the other hand, a failure to correctly describe the experimental data would either confirm the relevance of non-adiabatic effects in the dynamics or the lack of accuracy obtained with the exchange-correlation functional used. In this work, we present calculations that represent a first step in the direction of these objectives, since they include, apart from the six molecular degrees of freedom, the relevant surface phonons, and we also carry out a test on the influence of the density functional on the observables computed by performing the calculations with two density functionals.

Ab initio molecular dynamics (AIMD) has been employed to investigate gas-surface reactions since the early 90's [32–34]. However, the computational cost of AIMD limited these first studies to a few explorative trajectories. With the growth of computational power and the development of efficient algorithms, the use of AIMD to perform statistically relevant calculations of sticking probabilities for gas-surface reactions has recently become possible [35–37]. Advantages of this method lie in the 'on-the-fly' computation of the forces, since this strategy bypasses the need of pre-calculating and fitting a PES, with the possibility to model the effect of surface phonons through the inclusion of the motion of the surface atoms. Here, we apply the AIMD method to investigate the dissociation of N_2 on W(110), simulating the experimental surface temperature (800 K). In particular, we look at the effects that the explicit inclusion of surface temperature and surface motion have on the dissociation probability. Given the differences observed between dynamics on PESs computed with different exchange correlation functionals, both the PBE and RPBE functionals are tested with the AIMD method.

The AIMD results for N_2/W(110) are found to considerably differ from previous static surface results, especially at the lowest collision energies examined. The differences are due to a larger trapping-mediated (indirect) dissociation channel contribution observed in AIMD. An analysis of the trajectories reveals that a large portion of the molecules performing multiple rebounds on the surface are temporally trapped in areas of the energy landscape close to three configurations that correspond to potential wells of N_2 on an ideal surface, which may be associated with molecular adsorption states. These findings, together with the observation of a significant energy transfer from the

molecules to the lattice, suggest that the larger indirect dissociation channel contribution is due to molecules that are trapped in the potential wells and dissipate energy to phonons, such that they are not able to find their way back towards the gas phase and dissociation or molecular adsorption are the only possible outcomes. Both PBE- and RPBE-AIMD results are in qualitative agreement with experimental data at high collision energies, but they both fail to describe the experimental trend according to which the sticking probability monotonically increases with the initial collision energy (E_i). This failure, which is probably related to the overestimation of the indirect dissociation mechanism or molecular chemisorption, which dominate at low energies, might be caused by a wrong description given by both the PBE and the RPBE functionals of the area of the PES sampled by trapped molecules, in particular the area associated with molecular adsorption states.

This chapter is organized as follows: Section 7.2 describes the methodology; in section 7.3 we present and discuss our results, divided in four subsections: In 7.3.1 we discuss the molecular adsorption states that we observe on an ideal lattice; in 7.3.2 we present the results of our molecular beam simulations; in 7.3.3 we analyze the energy exchange between the molecule and the lattice; and in 7.3.4 we investigate the role that molecular adsorption plays in the chemisorption dynamics. Finally, the main conclusions are summarized in section 7.4.

7.2 Methods

The sticking probability of N_2 on W(110) has been determined using the AIMD technique [32, 35], following an implementation similar to the one described in Refs. [36, 37] and Chapters 3 and 5. Each sticking probability point has been determined from the computation of a set of 400 NVE trajectories (constant number of atoms, volume and total energy), representing single molecule-surface collisions. Trajectories belonging to the same set are characterized by the same initial normal translational energy for N_2. Our implementation exploits the quasi-classical trajectory method, in which vibrational zero-point energy is imparted to the N_2 molecules. The molecule's impact-site on the

surface, its vibrational phase and its orientation are randomly sampled using standard Monte-Carlo techniques, while the molecular angular momentum is set to zero. Only normal incidence scattering has been simulated. As in Ref. [12], the W(110) surface has been modeled by a periodic slab, using a 2x2 surface unit cell and 5 atomic layers. In order to model the experimental surface temperature (T_S = 800 K), the lattice constant has been taken as 1.0037 times the equilibrium DFT lattice constant, to account for the tungsten thermal expansion [38]. The equilibrium lattice constant values of 3.172 Å and 3.184 Å have been obtained from the optimization of the tungsten bulk primitive cell volume using the PBE functional and the RPBE functional, respectively. These values are in good agreement with the low-temperature experimental value of 3.163 Å [39] and with the previous calculations from Alducin et al. [12] and Bocan et al. [15].

In addition to accounting for the thermal expansion of the lattice, we model the experimental surface temperature by assigning velocities and displacements from the equilibrium positions to the surface atoms of the first four layers in a way similar to that used earlier in Ref. [36] and Chapter 3. Starting from initial displacements and velocities generated according to an independent harmonic oscillator model applied to the surface atoms of the uppermost four layers, we perform 1.5 ps long NVE equilibration runs for ten differently-initialized clean surfaces, using 1 fs as time-step. We have then performed a second 1 ps long NVE run for the ten equilibrated surfaces. The average surface temperatures computed for this second run are 723 (σ =113 K) and 728 (σ = 117 K) for PBE and RPBE, respectively, in reasonable agreement with the initially imposed temperature (i.e. 800 K, the experimental surface temperature). The surface initial conditions in the N_2/W(110) dynamics randomly sample the configurations (and the velocities) experienced during these second clean-surface runs.

We have also determined the root mean square displacements (RMSDs) for the tungsten atoms, averaging over all the moving atoms in the slab or considering only the first layer atoms (Table 7.1). The computed values are in reasonable agreement with the values extracted from clean surface equilibration runs performed with a larger (3x3) surface unit cell (PBE only, see also Table 7.1), the average surface temperature of

	All Atoms		Only First Layer	
Surface Unit Cell	2x2	3x3	2x2	3x3
PBE	0.154	0.147	0.185	0.177
RPBE	0.163	-	0.196	-

Table 7.1: Root mean square displacements (RMSD, in Å) of the surface atom positions calculated for the equilibration runs from which the surface initial conditions are extracted, for PBE and RPBE, and for a similar run with a larger surface unit cell (3x3, only PBE).

which is 779 K ($\sigma = 48$ K). From the model of Sears et al. [40], which has been fitted to neutron inelastic scattering measurements, we have computed a RMSD value for bulk tungsten equal to 0.129 Å at 800 K. Both Buchholz et al. [41] and Smith et al. [42] have observed a larger vibrational amplitude for the first layer atoms of a W(110) surface along the surface normal, the amplitude being a factor 1.4 to 2.6 larger than for bulk atoms. Smith et al. [42] also reported that no enhancement has been observed for the vibrational amplitude of the first layer atoms in the direction parallel to the surface. The measurements of Smith et al. were performed at a surface temperature of 300 K, while the data of Buchholz et al. were obtained from the analysis of data measured in a range of surface temperatures, not reported in Ref. [41]. If we assume the enhancement of the vibrational amplitude of the first layer surface atoms along the surface normal relative to the bulk vibrational amplitude to be independent on surface temperature, we can estimate the three dimensional first layer atom RMSD at 800 K to be in the range 0.148 Å to 0.220 Å which is in good agreement with the values that we have computed (Table 7.1).

All calculations have been performed with the DFT-AIMD code VASP [43–47]. Electronic structure calculations are characterized by a plane wave basis set with kinetic energy up to 400 eV, a 8x8x1 equally spaced Γ-centered first Brillouin zone sampling grid, a Fermi smearing with 0.1 eV width and the projected augmented wave (PAW) method [47,48] to represent the core electrons. Note that the PAW pseudopotential employed for tungsten has a Xe core, leaving six active electrons to be modeled explicitly (the valence electrons). A large vacuum space (13 Å) has been employed to separate the slab from its periodic images along the surface normal. We have verified that the residual

interaction energy for a molecule placed midway between two slabs with the bond length equal to its equilibrium value (our zero of energy) is lower than 10 meV. The influence of the exchange-correlation functional on the dynamics has been investigated by performing calculations with two GGA density functionals, i.e. PBE [49, 50] and RPBE [24]. Note that our computational setup is essentially the same as in Refs. [12, 15], with only small differences in the k-point grids and energy cut-offs for the plane wave expansion, the use of PAW pseudopotentials instead of ultrasoft pseudopotentials and the use of the PBE functional instead of the PW91 [22, 23] functional. Note, however, that the PBE functional has been designed to reproduce PW91 energies [49].

The AIMD trajectories have been integrated using the Verlet algorithm as implemented in VASP, employing a time-step of 1 fs and a maximum propagation time of 2.7 ps. The maximum propagation time, however, has been extended to 4.2 ps for the lowest initial collision energies investigated (0.9 eV and 1.3 eV), where the trapping-mediated dissociation mechanism dominates. In fact, molecules which are trapped can remain in this condition for several ps before dissociating, and therefore require longer time propagation. Given the larger computational cost of AIMD trajectories compared to the static-surface calculations, we cannot integrate AIMD calculations for longer times. The N_2 molecules, which are initially placed at 6 Å from the surface, are considered dissociated when the distance between the two N atoms becomes larger than 2 Å (the equilibrium N_2 bond length is 1.117 Å). In order to account at least in part for the possibility of scattering after barrier recrossing, we additionally require the distance between two atoms to become larger than the distance between one N atom and the closest periodic image of the other N atom. On the other hand, we consider a N_2 molecule to be scattered when Z, the distance between the surface and the center of mass (COM) of the molecule, becomes larger than 6 Å with the COM velocity pointing away from the surface. We label as 'unclear' the outcome of the trajectories in which the nitrogen molecule is neither scattered nor dissociated at the end of the propagation time (less than 7%, for each set of data).

Error bars presented in this article represent 68.3 % confidence intervals, and have

been estimated using the standard Wald interval [51]: for an estimated proportion p, e.g. a sticking probability value, for which $p = m/N$, where m is the number of reacted trajectories and N is the number of trajectories computed to estimate the proportion, $\sigma_p = \sqrt{p(1-p)/N}$.

Adsorption energies, which are defined as $E_a = -(\epsilon_{ads} - \epsilon_{asym})$, where ϵ_{ads} and ϵ_{asym} are the absolute energies of the adsorption system and of the configuration with N_2 at its equilibrium bond distance and at large distance from the surface, have been estimated for PBE and RPBE using an ideal slab optimized for the functional employed. The adsorption configurations have been obtained from geometry optimization procedures in which the lattice atoms have been kept fixed at the equilibrium slab geometry. Note that frequency analyses have confirmed that the results of geometry optimizations are true local minima, since no imaginary frequencies have been found. The adsorption energy values obtained with our computational setup have been compared to values from calculations with six additional active electrons included in the PAW pseudopotential description for tungsten, and to values from all-electron calculations. For the calculations with additional active electrons, the bulk tungsten lattice constant, the clean-slab interlayer distances and the adsorbate configurations have been re-optimized, but no considerable differences have been observed with respect to the geometries obtained for the PAW pseudopotential modeling only the valence electrons as active electrons. We have also increased the energy cutoff for the plane wave expansion to 600 eV, since the PAW pseudopotential with more active electrons employs a smaller cutoff radius for the pseudization sphere around the nucleus. The all-electron calculations have been performed with the FHI-AIMS package [52], using the 'tight' setting for the basis set size, for the same system geometry as optimized for the PAW with more active electrons.

In order to estimate the energy barriers that separate the molecular adsorption states from the dissociated state, we have performed nudged elastic band (NEB) calculations, using the VASP transition-state tools from Henkelman and Jónsson [53, 54]. Four images have been placed between the reactant configuration (the molecular adsorption geometry) and the product configuration (the dissociated configuration), and optimized

		X	Y	θ	ϕ	r	Z	E_a	Ref. [15]	Exp.
	Top	0	0	0	-	1.137	2.672	0.621	0.665 *	
PBE	Hollow	2.243	0	90	0	1.363	1.378	1.444	-	
	BH	3.657	1.264	74.48	-121.89	1.307	1.537	0.984	-	0.260,
	Top	0	0	0	-	1.141	2.694	0.385	0.389	0.450
RPBE	Hollow	2.251	0	90	0	1.370	1.391	0.972	-	
	BH	3.669	1.262	74.61	-122.27	1.316	1.544	0.543	-	

Table 7.2: Adsorption energies (eV) and geometries (r, Z, X and Y are in Å, θ and ϕ in degrees) for three minima corresponding to N_2 adsorption. Our adsorption energies are compared to the values of Ref. [15], and to experimental values from Refs. [3, 8]. Note that the value marked with (*) was obtained with the PW91 functional (not PBE).

through the fast inertial relaxation engine (FIRE) algorithm [55]. Through the use of climbing-image NEB (CI-NEB) calculations, the highest energy images are driven to the saddle points [53]. Calculations have been considered converged when all the forces are smaller than 20 meV/Å if not otherwise stated. Frequency analyses have confirmed that the highest energy images obtained are true first-order saddle points (only one imaginary frequency found).

7.3 Results and Discussion

7.3.1 Molecular Adsorption States

We identified three energetic minima that might be considered molecular adsorbed states for an ideal lattice. These minima are illustrated in Figure 7.1, and the corresponding adsorption energies and geometries are presented in Table 7.2 for both PBE and RPBE. Note that the adsorption energies calculated with PBE are always larger than the corresponding RPBE values, as expected from the more repulsive character of the latter [24].

As also described in Refs. [12,15], we find an adsorption well for N_2 placed above the top site at about 2.7 Å from the surface with the bond oriented perpendicular to the surface plane (top-vertical configuration). The adsorption energies that we determine for this configuration with PBE (0.621 eV) and RPBE (0.385 eV) reasonably reproduce the DFT values from Refs. [12,15] (0.665 eV and 0.389 eV, respectively), and differences should be expected due to the slightly different computational setups and, in one case,

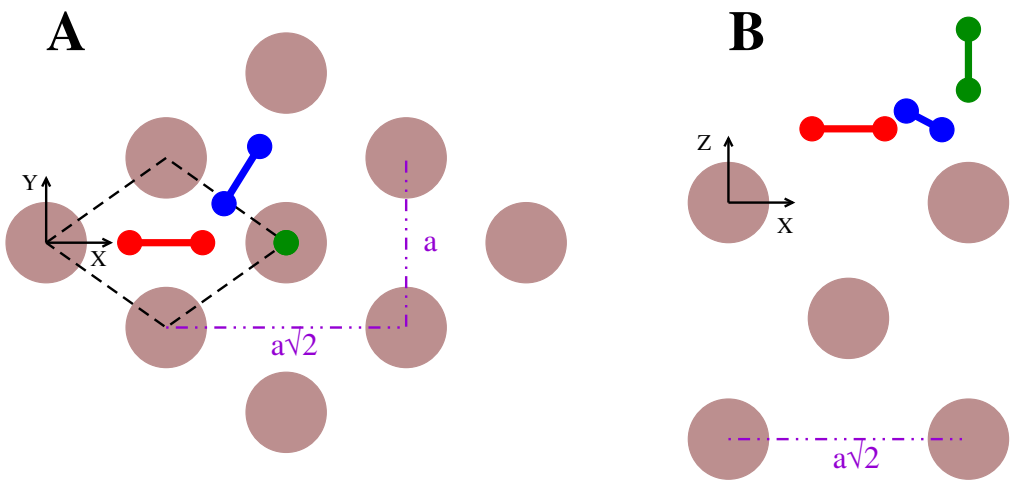

Figure 7.1: Graphical illustration of the molecular adsorption states: green for top-vertical, red for hollow-parallel and blue for bridge-hollow-tilted, using nomenclature as in the text. A and B represent bird's-eye and side views, respectively. Brown circles represent the surface atoms. The dashed black line delimits the surface unit cell.

the functional (PBE vs. PW91, see Section 7.2). In addition, we find two adsorption wells closer to the surface ($Z < 1.6$ Å). The first minimum is characterized by N_2 oriented parallel to the surface with its COM above the hollow site (hollow-parallel configuration). The adsorption energy is about 1.4 eV for PBE (1.0 eV for RPBE). Note that a similar adsorption geometry has been found on both Fe(110) [56] and Fe/W(110) [57], but the adsorption energy is larger on W(110). Note also the rather extended bond length of the adsorbed molecules with respect to the gas-phase value (about 20% longer). An additional molecular adsorption geometry has been found in the proximity of the bridge site, slightly shifted towards the hollow site, with one of the two N atoms approximately above the bridge site. The N_2 bond, slightly tilted from the parallel orientation ($\theta \approx 75°$), is almost perpendicular to the line connecting two adjacent top sites (bridge/hollow-tilted configuration). The adsorption energy at this site is intermediate between the hollow-parallel and the top-vertical geometries, about 1.0 eV and 0.5 eV for PBE and RPBE, respectively.

Figures 7.2 and 7.3 show two-dimensional (r, Z) potential energy plots for PBE and RPBE, respectively, in which the remaining molecular degrees of freedom are kept equal

Functional	Molecular Adsorption Geometry	E_b^{Ads}	E_b^{Diss}
PBE	Top-vertical	0.005	-0.432
	Hollow-parallel	0.406	-0.977
	Bridge/hollow-tilted	0.387	-0.486
RPBE	Top-vertical	0.071	-0.114
	Hollow-parallel	0.629	-0.550
	Bridge/hollow-tilted	0.610	-0.043

Table 7.3: The energy barriers experienced by the molecule when accessing the molecular adsorption wells (E_b^{Ads}) are compared to the barriers along the minimum energy paths that connect each of the molecular adsorption configurations to the dissociated configuration (E_b^{Diss}), in eV. Note that the E_b^{Ads} values refer to the barriers in the 2D plots in Figure 7.2 and in Figure 7.3, while the E_b^{Diss} values have been computed through CI-NEB calculations, and are therefore first order saddle points in the six-dimensional space of the N_2 configurations. The zero of energy is defined as the energy of the molecule in its equilibrium geometry placed midway between two slabs.

to the values corresponding to the three molecular adsorption geometries described. As for the calculation of the molecular adsorption energies, the surface atoms have been kept in their equilibrium configuration. Alducin et al. [12, 13] and Bocan et al. [15] noted that the access to the top-vertical adsorption geometry is barrier-less if the PW91 functional is employed, while the RPBE functional predicts a barrier of about 80 meV. Similarly, along the same path, at about 3.7 Å from the surface, we have found a barrier of about 70 meV when using the RPBE functional (Table 7.3 and Figure 7.3A). Using the PBE functional, we find a very small barrier (about 5 meV) at $Z = 4$ Å (see Figure 7.4, blue symbols, and Table 7.3) where the PW91-PES from Refs. [12, 13] returns an interaction energy of about -5 meV (Figure 3 of Ref. [12]). We verified that in our computational setup a small barrier (which is, however, less than 1 meV high) is still present even after adding 10 Å of vacuum along the surface normal and after shifting the asymptotic configuration further from the surface (see Figure 7.4, red symbols), which suggests that the observed barrier is not an 'artifact' of residual attractive interactions for the asymptotic configuration (our zero of energy). The size of this barrier, however, is negligible when compared to the collision energies that we have investigated (0.9 eV or larger), therefore we do not expect differences in the dynamics due to the absence of a non-activated path, which characterizes the PW91-PES from Refs. [12, 13].

For what concerns the other two molecular adsorption geometries, a barrier is en-

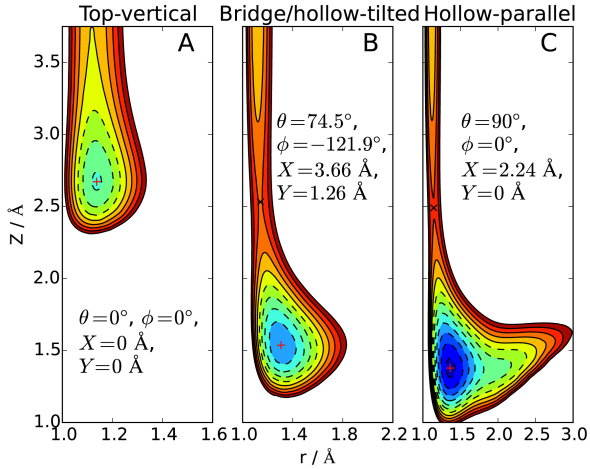

Figure 7.2: The PBE interaction energy is plotted as a function of r and Z for the three configurations corresponding to the molecular adsorption geometries. The position of the adsorption geometries is indicated in the plots by a red +, and a black × indicates the position of the saddle point in the entrance channel. Interaction energies have been evaluated on a dense grid in r and Z and spline interpolated for illustration purposes. Contour lines separate 0.2 eV energy intervals up to a maximum of 0.8 eV. Dashed lines identify negative energy values.

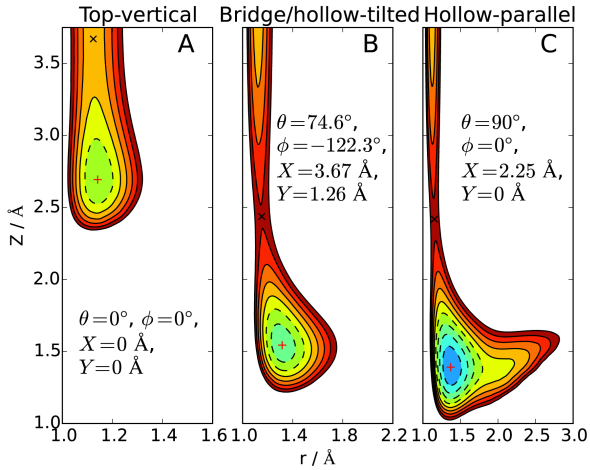

Figure 7.3: Same as Figure 7.2, but for RPBE.

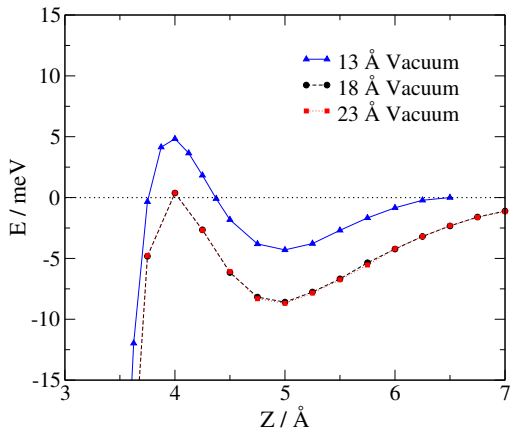

Figure 7.4: The PBE interaction energy is plotted as a function of Z, using the same equilibrium 5-layer slab to model the W(110) surface, but using different vacuum spaces along the surface normal. The N_2 bond length has been kept equal to the equilibrium value of 1.117 Å. The zero of energy is defined as the energy of the molecule in its equilibrium geometry placed midway between two slabs.

countered in the access to the adsorption wells from the gas-phase, independently of which functional is employed (Figure 7.2B-7.2C, Figure 7.3B-7.3C and Table 7.3). To enter both the bridge/hollow-tilted and the hollow-parallel adsorption wells, the saddle points that the molecule has to overcome in the 2D-cuts in Figure 7.2 and 7.3 are located between 2.4 and 2.6 Å from the surface. The height of the barrier is about 0.6 eV for RPBE, and only about 0.4 eV for PBE. Note that all the mentioned barriers are lower than the minimum collision energy simulated (0.9 eV).

The configurations of the hollow-parallel and of the bridge/hollow-tilted adsorption geometries were not part of the set of configurations that have been interpolated in the PES employed in Refs. [12] and [15]. However, elbow plots computed for these PESs for the configurations corresponding to the hollow-parallel and bridge/hollow-tilted molecular adsorption states reveal features similar to the plots in Figure 7.2 and 7.3 [58]. For the hollow-parallel configuration, the bottoms of the adsorption wells are located at $r \sim 1.4-1.5$ Å and $Z \sim 1.4$ Å, with interaction energy values of 1.916 eV and 1.313 eV for PW91 and RPBE, respectively (cf. Table 7.2). For the bridge/hollow-tilted configuration, the minima in the 2D-cuts are located at $r \sim 1.3$ Å and $Z \sim 1.6$ Å, with the interaction energy being 0.670 eV and 0.205 eV for PW91 and RPBE, respectively

PBE	W PAW 6 v.e.	W PAW 12 v.e.	AE
Top-vertical	0.621	0.604	0.640
Hollow-parallel	1.444	1.368	1.360
Bridge/hollow-tilted	0.984	0.919	0.943

Table 7.4: Adsorption energies (eV) for the three identified molecular adsorption geometries, for PBE. The results obtained using the PAW pseudopotential that includes 6 valence electron for W are compared to the results obtained using the PAW pseudopotential that includes 12 valence electron (i.e. including the six 5p electrons). Adsorption energies are also compared to results of all electron (AE) calculations.

(cf. Table 7.2). Therefore, the positions of the minima agree reasonably well with the positions of the minima that we have found. The well depths, however, can differ up to almost 0.5 eV (for the hollow-parallel configurations with PW91), with the hollow-parallel (bridge/hollow-tilted) adsorption energies in the PESs being larger (smaller) than the values that we have determined. Note, however, that these analyses have been based on the two dimensional (r, Z)-cuts of the PESs only [58]; we do not know whether these represent 'true' minima in the full dimensional PESs.

Adsorption energies calculated using more active electrons in conjunction with the PAW pseudopotential for tungsten are reported in Tables 7.4 and 7.5 for PBE and RPBE, respectively. The adsorption energy values differ from our computational setup values by no more than 80 meV. Note that we have measured an increase in the computational cost when going from six to twelve active electrons of about a factor 2 for single point energy calculations. Table 7.4 and Table 7.5 also report all-electron adsorption energy values, which compare reasonably well with the adsorption energies computed using our computational setup: differences range from 7 meV for the RPBE top-vertical adsorption geometry to less than 130 meV for the RPBE hollow-parallel geometry. In the light of these results, we are confident that the pseudopotentials employed in our computational setup are able to capture with reasonable accuracy the effect of the presence of the deep adsorption wells predicted by the PBE and RPBE functionals for this system, at a relatively low computational cost.

Experimentally, N_2 is known to molecularly adsorb on W(110) in the so-called γ adsorption state, with estimates of the adsorption energy of 0.260 eV [3] and 0.450

RPBE	W PAW 6 v.e.	W PAW 12 v.e.	AE
Top-vertical	0.385	0.366	0.378
Hollow-parallel	0.972	0.895	0.850
Bridge/hollow-tilted	0.542	0.479	0.466

Table 7.5: Same as Table 7.4, but for RPBE.

eV [8]. Note that another molecular adsorption state, α-N_2, with larger adsorption energy (about 0.8 eV), has been observed on tungsten surfaces [59], but not on the (110) crystal face [2]. The experimental molecular adsorption energies for γ-N_2 are much smaller than the theoretical predictions. Only the top-vertical adsorption energy computed with the RPBE functional is comparable to the experimental estimates for γ-N_2, as already noted by Bocan et al. [15]. However, both Lin et al. [7] and Zhang et al. [8] suggested the presence of a molecular adsorption state different from the γ-N_2 state for N_2 + W(110). In particular, Zhang et al. [8] found some evidence for a δ-N_2 state, populated through electron bombardment of γ-N_2. According to the authors, this molecular adsorption state does not desorb through further electron impact, but can be dissociated to atomic N. The authors also suggested a "lying down" adsorption geometry for this state, and a N-N bond length "abnormally long" [8]. Analogies with the hollow-parallel adsorption geometry that we have identified using both the PBE and the RPBE functionals are evident. However, no significant differences have been found between thermal programmed desorption (TPD) spectra recorded for δ-N_2 and for γ-N_2, and the authors interpreted this finding as a similar desorption activation energy for the two molecular adsorption states, or a possible conversion of δ-N_2 to γ-N_2 before desorption. Our calculations, on the other hand, suggest a rather large difference in adsorption energies between top-vertical and hollow-parallel adsorption states.

We have performed CI-NEB calculations in order to find the minimum energy paths (MEPs) connecting the molecularly adsorbed states to the dissociated configuration (see Appendix 7.A.1). While the most stable adsorption site for one N atom on the W(110) surface is found to be the four fold hollow site, as already noted by Alducin et al. [12], we find that the configuration with two N atoms adsorbed in two adjacent hollow sites is stabilized, within the 2x2 surface unit cell employed, by a 0.5 Å shift of both atoms

in the same direction towards the neighboring long top-hollow sites. This configuration has been used as the product state for the CI-NEB calculations. In Table 7.3, we report the barriers computed with respect to the configuration with N_2 at its equilibrium bond distance at large distance from the surface. For all the MEPs analyzed, we observe that the molecule can dissociate without any barrier with respect to the gas-phase, since the dissociation barriers of Table 7.3 are negative in all cases when going from the molecular to the dissociative chemisorption well. For the PBE functional, the energy required to move from the bridge/hollow-tilted and the hollow-parallel adsorption configurations towards dissociation are about 0.50 eV and 0.47 eV, respectively, with respect to the bottom of the molecular adsorption wells. For the RPBE functional, the barrier along the path that connects the bridge/hollow-tilted geometry to dissociation is also 0.50 eV, while a slightly lower barrier (0.42 eV) is found for dissociating molecules adsorbed in the hollow-parallel configuration.

For the MEP connecting the top-vertical adsorption geometry to the dissociated state we found that the potential is quite flat in the proximity of the barrier. Therefore, a small amount of noise in the forces can drive the images away from the MEP and we were not able to converge all the forces below 40 meV/Å. For the PBE path, CI-NEB calculations only converged when allowing the highest-energy image to be optimized while the other images were frozen in the configurations optimized with regular NEB calculations (without CI). The barriers observed along this path are about 0.20 eV and 0.27 eV for PBE and RPBE, respectively, with respect to the bottom of the molecular adsorption well.

7.3.2 Sticking Probability

The N_2 sticking (dissociation) probability computed with AIMD is plotted in Figure 7.5 as a function of the initial collision energy. In the same figure, two sets of experimental data have been reported [5, 9], as a measure of the uncertainty of the experimental values. The agreement between both PBE- and RPBE-AIMD results and experimental data is semi-quantitative at the high collision energies. However, AIMD overestimates

the experimental sticking probability at low collision energies. Note that the AIMD method predicts a reaction probability that does not depend on E_i, failing to reproduce the experimental trend according to which the dissociation probability monotonically increases with increasing collision energy.

For both the PBE and the RPBE functionals, the AIMD probabilities are considerably larger than the probabilities obtained in the previous static-surface study, in particular at the lowest collision energies, where probabilities differ by more than a factor two. These discrepancies cannot be due to the small differences in the computational setups, listed in section 7.2. Note that the previous static surface study implemented the classical-trajectory (CT) method, while our AIMD calculations make use of a QCT approach. However, differences between the QCT and CT reaction probabilities have been found to be small (less than 5%) for this system, in the range of collision energies examined [12]. Furthermore, we have performed AIMD calculations simulating an ideal frozen surface (AIMD-IF), using the PBE functional, at a collision energy of 1.3 eV (Figure 7.5) and the computed dissociation probability reproduces (within error bars) the value from the previous PW91 static surface study [12]. Therefore, the inclusion of surface temperature effects (i.e., lattice distortion) or surface motion effects (for instance, recoil) or a combination of the two in the calculations has to be responsible for the mismatch between the present AIMD results and the previous static surface study.

In order to shed light on the main factor that is responsible for the sticking probability increase with respect to static surface data, we have performed AIMD calculations simulating a distorted lattice as in the moving surface calculations, but keeping the surface atoms frozen at their initial positions, thereby blocking energy transfer to the surface (AIMD on a distorted frozen lattice, AIMD-DF). We have computed one sticking probability point for the collision energy and density functional at which the largest discrepancy from static surface calculations was observed (E_i = 0.9 eV, PBE). The computed dissociation probability does not considerably differ from the previous PW91 static surface data, suggesting a much larger influence of surface motion effects (energy transfer to the lattice) than of 'static' lattice distortion effects.

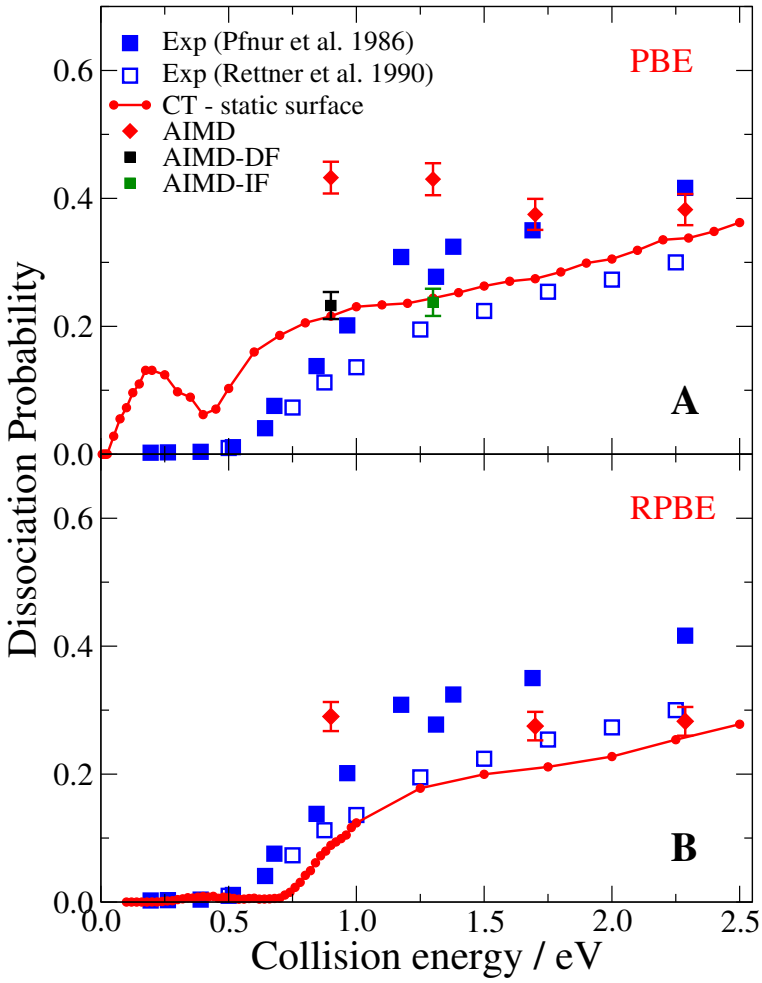

Figure 7.5: Dissociation probability as a function of the initial collision energy. AIMD moving-surface results (AIMD, diamonds) are compared to experimental data (blue squares, solid from Ref. [5] and empty from Ref. [9]) and to previous static-surface CT calculations [15]. The dissociation probability values computed using AIMD, simulating an ideal frozen surface (AIMD-IF, green) and simulating a distorted frozen surface (AIMD-DF, black) are also reported. In A, all AIMD calculations employed the PBE functional and the CT calculations the PW91 functional, while in B the RPBE functional has been employed by both AIMD and CT calculations.

The analysis of our moving surface calculations shows that the dissociation of N_2 can occur either at the first impact on the surface or after many rebounds, as already observed by Alducin et al. [12]. In that study the dissociation was separated into a direct and a trapping-mediated (indirect) contribution, defined on the basis of the number of rebounds that the molecules experience before dissociation (less than four and more than three, respectively). The direct mechanism was found to become more and more relevant with increasing E_i, while the indirect mechanism, dominant at low energies, was found to have a small contribution at high energies. Adopting the same definition [12] for the direct and the indirect dissociation channels, we observe the same trend in our AIMD study, for both the PBE and the RPBE functional (see Figure 7.6A and 7.6B, respectively). The direct mechanism accounts for about one third of the reactivity at 0.9 eV and two thirds at 2.287 eV. Note that the direct dissociation probabilities computed with PBE-AIMD are similar to the direct dissociation probabilities from the previous PW91 static surface study, while the indirect dissociation probabilities are considerably larger for AIMD. Note also that AIMD-DF direct and indirect dissociation probabilities (Figure 7.6A) reproduce reasonably well the corresponding static surface values, suggesting that surface motion effects (energy transfer) constitute the main factor responsible for the larger trapping-mediated dissociation probability observed in AIMD.

Upper-bounds to the AIMD dissociation probabilities, calculated assuming that all the molecules of which the outcome is still unclear at the end of the propagation time (neither dissociated nor scattered) would in the end dissociate, slightly increase the indirect dissociation channel, but are not dramatically different from the actual dissociation probabilities. Therefore, the trends that we discuss should not be affected by additional dissociation upon longer time propagation.

As shown in Figure 7.6C and 7.6D, the decrease of the indirect dissociation probability is due to a decreased trapping probability, whereas, interestingly, the dissociation probability of the trapped molecules does not depend on the initial collision energy E_i. This is consistent with a model in which the higher the collision energy is, the larger is the number of available direct paths for dissociation (more direct reaction) and the lower

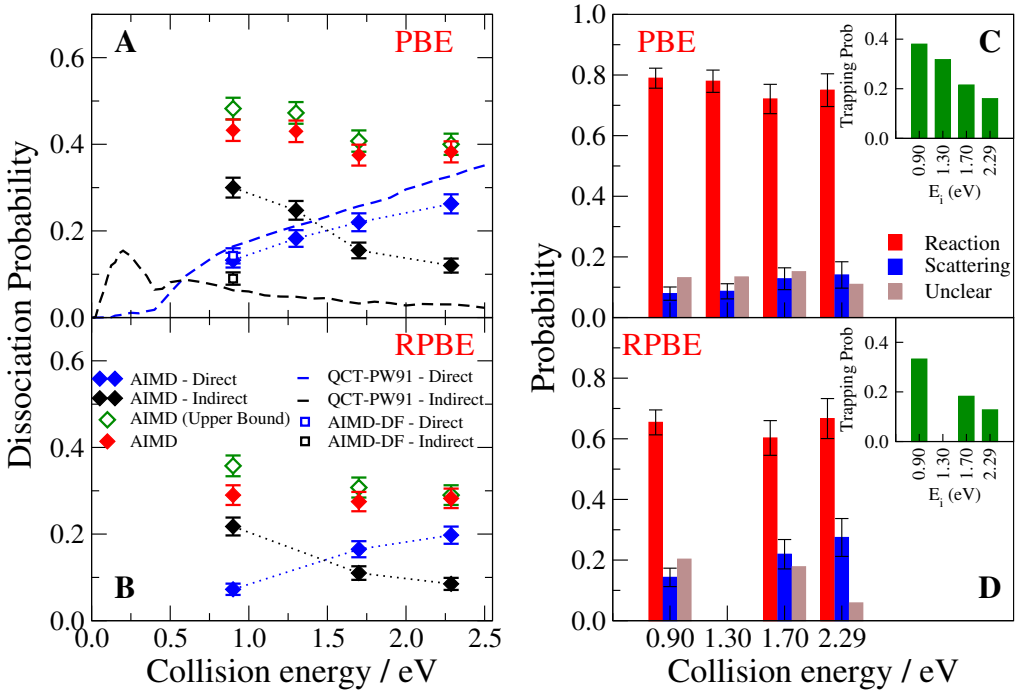

Figure 7.6: A-B: The direct (blue diamonds) and trapping-mediated (black diamonds) contributions to the dissociation probability (full red diamonds) obtained with AIMD are plotted as a function of E_i. The upper bound for the dissociation probabilities is also provided (empty green diamonds), assuming that all the unclear trajectories will dissociate. Direct and indirect dissociation probabilities for AIMD calculations simulating a distorted frozen surface (AIMD-DF) are plotted as empty blue and black squares, respectively. The direct and trapping-mediated contributions to the dissociation probability determined in the previous static-surface QCT study [12] are also plotted as dashed lines for comparison. In A, the AIMD employed the PBE functional and the QCT calculations the PW91 functional, while in B the RPBE functional has been employed in the AIMD. C-D: Reaction and scattering probabilities for trapped molecules are plotted as red and blue bars, respectively. The fraction of trapped molecules that are neither dissociated nor scattered at the end of the propagation time is plotted in brown. In the insets, the trapping probability as a function of E_i. C is for PBE, D is for RPBE.

is the probability that a molecule would be stabilized in an adsorption state (resulting in less indirect reaction). As a result of the increasing direct reaction probability and the decreasing indirect reaction probability with increasing E_i, the total reaction probability remains more or less constant. We note in passing that the reaction probability of the trapped molecules is larger for PBE than for RPBE.

7.3.3 Energy Transfer to the Lattice

In order to better understand trapping, we have looked at the energy exchanged between the molecules and the surface. For the scattered trajectories, a significant amount of energy is transferred from the molecules to the lattice, as visible from the energy transfer distributions in Figure 7.7A and 7.7B for PBE and RPBE, respectively. Quite broad distributions are observed, with negative energy tails representing energy transferred from the surface to the molecules, without significant differences between PBE and RPBE data. Note that the higher the initial collision energy, the broader and the more shifted to high energies the distributions are. Note also that the larger energy transfer directed from the molecules to the surface is consistent with the fact that surface atoms only possess thermal energy, while much more (collision) energy is initially available in the molecules.

Average energy transfer values are reported in Table 7.6 and Table 7.7 for PBE and RPBE, respectively. The average energy transfer with a single collision, $\langle \Delta E \rangle_1$, is about 20% of E_i. The observed values of $\langle \Delta E \rangle_1$ are considerably lower than the estimates obtained on the basis of the Baule model [60, 61], which are reported in Table 7.8. According to this model, which assumes the molecule-surface impact to be equivalent to the collision of two hard-spheres, the energy transferred to the lattice is:

$$\Delta E = \frac{4\mu}{(1+\mu)^2} E_i, \tag{7.1}$$

where μ is the ratio between the molecular (projectile) mass and the mass of one surface atom M_W. For a system for which the molecular adsorption energy V is non-negligible,

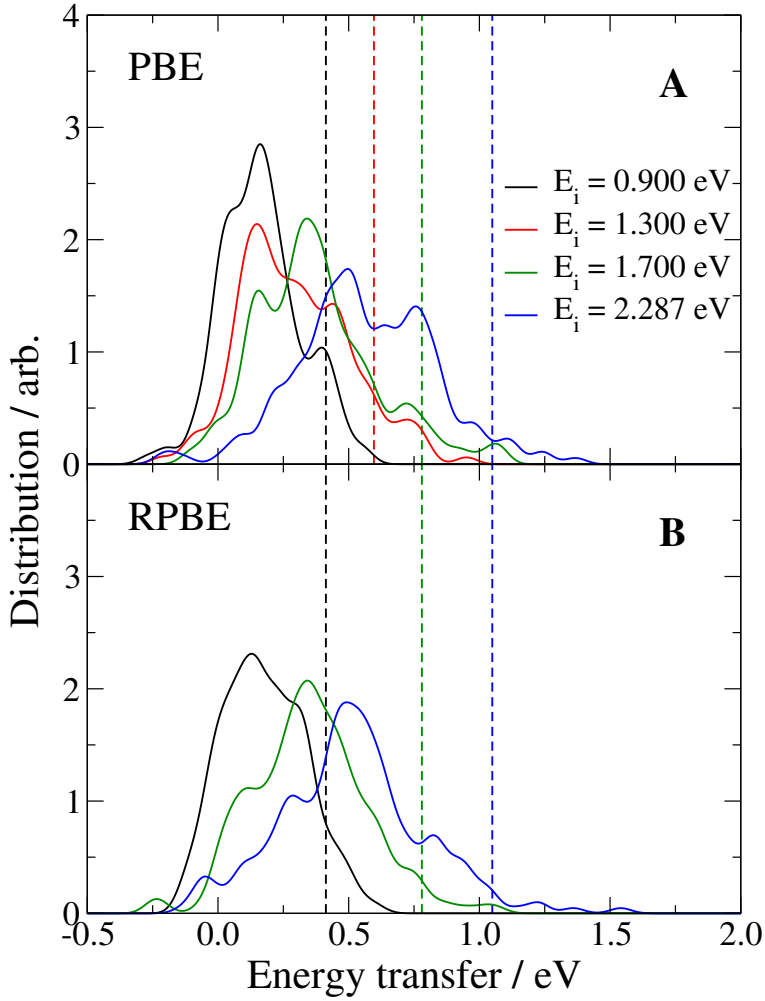

Figure 7.7: Energy transfer distributions computed for molecules scattered without performing any rebound on the surface are plotted as solid lines. Smooth distributions have been obtained by summing Gaussian functions centered at the computed energy distribution values with a σ parameter equal to 40 meV. The energy transfer values according to the Baule model are plotted as vertical dashed lines. Different colors correspond to the various initial collision energies: black for 0.9 eV, red for 1.3 eV, green for 1.7 eV and blue for 2.287 eV. A is for PBE and B is for RPBE.

PBE	$\langle \Delta E \rangle$			
E_i(eV)	0 Rebounds	>0 Rebounds	All	α
0.900	0.166± 0.012 (151)	0.344 ± 0.025 (56)	0.214 ± 0.013 (207)	0.269 ± 0.016
1.300	0.299± 0.016 (164)	0.517 ± 0.039 (47)	0.348 ± 0.017 (211)	0.291 ± 0.014
1.700	0.376 ± 0.017 (180)	0.820 ± 0.050 (57)	0.483 ± 0.022 (237)	0.303 ± 0.014
2.287	0.565 ± 0.020 (183)	0.938 ± 0.054 (57)	0.654 ± 0.022 (240)	0.300 ± 0.010

Table 7.6: Average energy transfer to the lattice ($\langle \Delta E \rangle$, eV) evaluated for the molecules scattered with no rebounds on the surface, for the molecules scattered after one or more rebounds, and for all the molecules. The calculated accommodation coefficient α is also reported. Standard errors of the mean are presented together with the number of scattered trajectories for each set of data (in brackets). The data refer to PBE calculations.

like N_2/W(110), E_i is usually replaced by $E_i + V$ in Eq. 7.1, in order to account for the extra kinetic energy that a molecule acquires when flying over the potential well (modified Baule model). The energy transfer values predicted by the modified Baule model, assuming V to be equal to the largest adsorption energy computed (i.e. for the hollow-parallel configuration, see Tables 7.4 and 7.5), are also reported in Table 7.8. The ΔE values predicted by the modified Baule model are even larger than the values predicted by the standard Baule model, and therefore in even worse agreement with the values found in AIMD. Due to the large adsorption energies ($E_a = 1.4$ eV with PBE), the modified Baule model even predicts an energy transfer larger than the initial collision energy for PBE at $E_i = 0.9$ eV. Given the simplicity of the (modified) Baule model, it is not surprising that discrepancies with AIMD results are observed. An effective surface atom mass can be obtained by fitting Eq. 7.1 to the computed ΔE values using the surface atom mass atom as a free parameter. This fit returns an effective surface atom mass equal to 2.4 M_W for the case in which the presence of a potential well is neglected, while a value of 4.7 (4.1) M_W is obtained if we consider V to be equal to the largest adsorption energy observed with the PBE (RPBE) functional. Effective surface atom mass values significantly different from M_W indicate a behaviour of the lattice quite far from the independent hard-sphere model, as expected for close packed surfaces.

The average energy transfer values computed for the trajectories that experience more than one rebound on the surface are considerably larger than the corresponding

RPBE	$\langle \Delta E \rangle$			
E_i(eV)	0 Rebounds	>0 Rebounds	All	α
0.900	0.178 ± 0.011 (186)	0.296 ± 0.024 (69)	0.210 ± 0.011 (257)	0.264 ± 0.014
1.700	0.351 ± 0.015 (217)	0.806 ± 0.046 (60)	0.450 ± 0.019 (277)	0.282 ± 0.012
2.287	0.512 ± 0.019 (216)	0.975 ± 0.047 (68)	0.623 ± 0.022 (284)	0.285 ± 0.010

Table 7.7: Same as Table 7.6, but for RPBE.

E_i(eV)	Baule	Modified Baule ($V = E_a^{PBE}$)	Modified Baule ($V = E_a^{RPBE}$)
0.900	0.413	1.075	0.859
1.300	0.596	1.259	1.042
1.700	0.780	1.443	1.226
2.287	1.049	1.712	1.495

Table 7.8: Energy transfer (eV) estimated using the Baule model, or modified Baule model, using as adsorption energy the largest PBE and RPBE adsorption energies, respectively.

$\langle \Delta E \rangle_1$ values, as expected for multiple collisions. The energy transfer averaged over all scattered trajectories amounts to about 25% of the initial collision energy, in good agreement with the findings of Pétuya et al. [21], who looked at the non-reactive scattering of N_2 from a different tungsten surface (W(100)) and included dissipation to phonons using the GLO method.

An experimental observable related to the energy transfer to the lattice is the accommodation coefficient α, defined as the average energy that a molecule exchanges with the surface divided by the difference between the average collision energy of the molecules and the translational energy that they would have if they would be in thermal equilibrium with the surface [62]:

$$\alpha = \frac{\langle \Delta E \rangle}{E_i - \frac{3}{2} k_b T_s}. \tag{7.2}$$

Thermal accommodation coefficients for nitrogen on tungsten have been determined by Chen and Saxena [63,64] using a heat-transfer column apparatus. They have determined the heat transfer from a heated gas-covered tungsten wire to the surrounding nitrogen gas, and calculated an accommodation coefficient in the range 0.18-0.32 for a surface temperature of 850 K. From our calculations, we extract a value of α in the range 0.26-

0.30 (Table 7.6 and Table 7.7), in reasonable agreement with the experimental data. However, we want to stress the fact that experimental conditions are quite far from the ones that we are simulating: the tungsten wire is not a well-cut single crystal and the gas pressures at which they have worked are relatively high (100-400 mbar). Furthermore, the authors report the possible presence of nitrogen atoms and oxygen impurities on the surfaces.

Hanisco et al. investigated the rotationally inelastic scattering of N_2 from W(110) ($T_s = 1200$ K) [10]. They determined the total (rotational + translational) final energy E_f for various final rotational states, for normal incidence and normal detection, for two different initial collision energies E_i. For $E_i = 0.75$ eV they also reported the average fraction of energy retained by the molecules $\langle E_f/E_i \rangle = 0.68$. Given the computational cost of AIMD, the number of simulated trajectories is limited, and we cannot compute theoretical final-state-resolved data with satisfying statistical accuracy. The value of $\langle E_f/E_i \rangle$ that we compute for the lowest collision energy simulated ($E_i = 0.90$ eV), assuming an acceptance angle $\Theta = 20°$ from the surface normal, is 0.82 ± 0.02 (0.80 ± 0.02) with PBE (RPBE). Note that considering only the trajectories in which the final vibrational energy does not differ from the (initial) vibrational zero point energy by more that 15% does not change the computed values of $\langle E_f/E_i \rangle$ by more than 3%. The comparison with the experimental value of $\langle E_f/E_i \rangle$ suggests that AIMD is somewhat underestimating the energy transfer to surface phonons.

Significant energy transfer to the lattice also occurs in the reactive trajectories. Figure 7.8 shows the time evolution of the mean kinetic energy of the trapped molecules that react at $t \geqslant 800$ fs. The mean kinetic energy of the molecules decreases rapidly as a function of time, and at $t = 800$ fs, the molecules have lost a large part of their initial kinetic energy, due to multiple collisions with the surface atoms. Since we are forced to employ a slab of limited thickness in the calculations and since the total energy of each AIMD trajectory is constant, energy transfer to the lattice could cause a non-physical heating of the surface. Such a surface temperature increase, however, would not be a concern if the energy flow from the impact site of the molecule to the boundaries of the

surface unit cell and back to the molecule would be slower than the dissociation event. Figure 7.9 shows the mean kinetic energy of each atomic layer of the slab as a function of time, for the PBE-AIMD trajectories that react at $t \geqslant 800$ fs for $E_i = 0.9$ eV. The same behaviour is observed for RPBE-AIMD and for the other initial collision energies (not shown), but statistics are poorer as the trapping-mediated dissociation channel decreases in importance with increasing E_i. As expected, the first layer atoms on average undergo a sudden increase of kinetic energy upon collision of the molecule with the surface, at about 175 fs. The layers below experience smoother changes in kinetic energy, and these changes occur at larger times. The fourth layer is almost unperturbed even after several hundreds of fs after the impact of the molecule. These observations suggest that our finite-size slab is thick enough not to observe significant nonphysical energy reflection from the bottom of the slab on the examined time-scale. Note that by 1 ps, almost 70% of the dissociation observed for $E_i = 0.9$ eV, for which the trapping mediated reaction has the largest contribution, has already occurred. Therefore, applying a thermostat to the atoms at the boundary of the cell in order to avoid non-physical phonon reflection is not expected to considerably affect the dynamics of the majority of the dissociating molecules. Moreover, for the minority of the molecules dissociating at larger times, which might be affected by a surface being non-physically 'too hot', the use of a thermostat would facilitate the energy flow from the molecule to the surface. This would make it even more difficult for them to 'escape' from the adsorption wells, increasing even more the sticking probability. Therefore, applying a thermostat to the bottommost moving layer might be necessary to accurately describe the behaviour of the molecules dissociating at large times, but we do not expect this to change the most important conclusions of our study.

Another observation from Figure 7.8 is that at 800 fs the average kinetic energy of the molecules that go on to react is almost independent of the initial collision energy. If the molecules would be in thermal equilibrium with an infinite surface, their expected mean kinetic energy would be $3k_bT_S$ (about 0.2 eV for $T_S = 800$ K, also plotted as a horizontal dash in Figure 7.8). The observed average kinetic energy is about 0.6 eV,

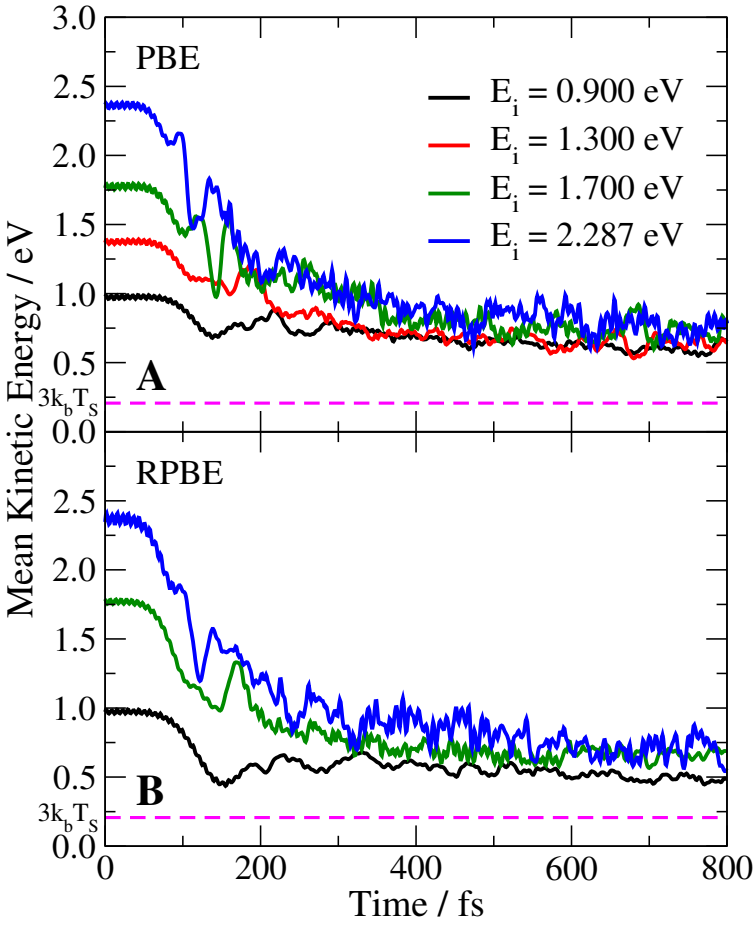

Figure 7.8: The mean kinetic energy of the molecules dissociating at propagation times larger than 800 fs is plotted as a function of time. A is for PBE and B is for RPBE. Colors are as for Figure 7.7. The dashed horizontal line indicates the energy corresponding to $3k_bT_s$.

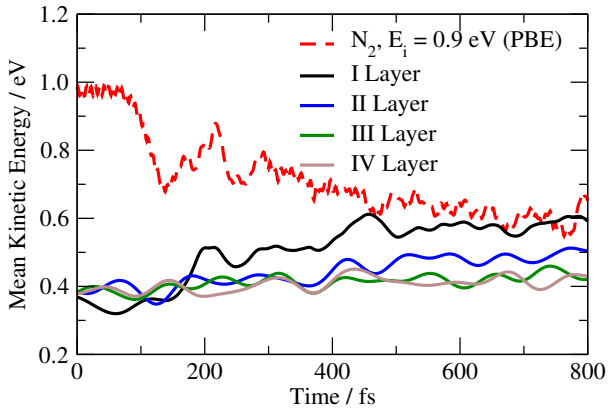

Figure 7.9: The mean kinetic energies evaluated for the PBE trajectories with $E_i = 0.9$ eV dissociating at propagation times larger than 800 fs is plotted as a function of time. The dashed red line corresponds to the mean kinetic energy of the molecule, while black, blue, green and brown solid lines correspond to the mean kinetic energy of the first, second, third and fourth atomic layers, respectively.

which is considerably higher than this thermal limit. However, this can be explained considering that energy transferred from the molecule to the slab generates a 'hot' first layer, which has not yet had enough time to equilibrate with the rest of the slab, as shown in Figure 7.9.

The fast energy transfer from the molecule to the surface explains the insensitivity of the dissociation probability of the trapped molecules to the initial collision energy. Trapped molecules quickly dissipate energy to phonons so that similar amounts of energy remain available for the reaction, regardless of the initial E_i. Fast energy transfer to the lattice, together with the role played by the molecular adsorption states, can also explain why a larger indirect dissociation probability is obtained with AIMD than in previous static surface studies, as shown in Section 7.3.4.

7.3.4 The Role of Molecular Adsorption in the Dynamics

We analyzed the configurational space explored by the N_2 molecules that undergo molecular trapping. In particular, we looked for the configurations that might be attributed to the molecular adsorption states identified on an ideal surface. Note that all the molecular adsorption wells can be directly accessed from the gas-phase at all the considered

collision energies, since the minimum energy barriers for accessing these wells are lower than the collision energies examined for both the PBE and RPBE functionals (see Table 7.3, Figure 7.2 and Figure 7.3).

Instantaneous surface deformations due to the thermal displacements of the surface atoms might slightly modify the geometry (and the energy) of the molecular adsorption states. Also for this reason, operational definitions that include ranges of molecular coordinates have been used to determine whether the molecule assumes the configuration of a specific adsorption state. We defined the top-vertical adsorption state as exhibiting configurations with the molecule's COM above a first layer surface atom, within a lateral displacement of 0.5 Å and Z and θ within 0.2 Å and 20° from the ideal lattice adsorption state values (see Table 7.2), respectively. Note that the large tolerance that we allow for the lateral displacement is justified by the relatively low corrugation of the PES in X and Y close to this minimum: A displacement of N_2 of 0.5 Å away from the top-site would increase the interaction energy by less than 0.18 eV, for both functionals. The same tolerance in Z and θ was employed for identifying the other two molecular adsorption states. For the hollow-parallel adsorption state the molecule's COM was required to be within a lateral displacement of 0.25 Å from the second layer atom and ϕ to assume a value within 20° from the ideal lattice adsorption state value (see Table 7.2), taking the N_2 inversion symmetry into account. Finally, for the bridge/hollow-tilted configuration, the azimuthal angle ϕ has been required to be perpendicular to the line connecting two adjacent top sites (within 20°), with one of the two N atoms above the bridge site (within a 0.25 Å lateral displacement). Note that the use of tolerance intervals 50 % larger than the employed ones did not considerably affect the analysis.

We find that trapped molecules that go on to react or whose outcome is still unclear at the end of the propagation often visit one or more of the two deepest molecular adsorption states: The hollow-parallel configuration is visited in more than 50 % of the cases, and the bridge/hollow-tilted configuration is visited in more than 60 % of the cases, for both PBE and RPBE. This is not the case for the molecules that will in the end be scattered. In particular, the molecules that reach the hollow-parallel configuration

(the deepest adsorption well) are almost never scattered: This event is observed only in one out of 211 trajectories for the PBE calculations, at the highest E_i, and very few times (in 4 out of 122 trajectories, one for $E_i = 1.7$ eV and three for $E_i = 2.287$ eV) for the RPBE calculations. Furthermore, most of the trapped molecules that will eventually react (70% or more, depending on the initial collision energy) visit at least one of the molecular adsorption states before dissociation.

These findings suggest the following picture of the computed dynamics: molecules reaching one of the molecular adsorption states are often (temporally) trapped. From these adsorption states, molecules dissipate energy to the phonons so that retracing the path back towards the gas phase is more difficult or even impossible; dissociation and molecular adsorption are then the only possible outcomes for these molecules. The energy dissipation to phonons therefore enhances the trapping-mediated dissociation channel, and this explains the larger contribution of the indirect mechanism to dissociation observed in AIMD than seen in static-surface calculations [12, 13, 15] and in AIMD-DF calculations. In this picture, the fact that AIMD overestimates the experimental dissociation probabilities at low E_i is consistent with the overestimation of the molecular adsorption energies by both PBE and RPBE, as discussed in Section 7.3.1. With shallower adsorption wells the trapping probability will be reduced and, as a consequence, so will the trapping mediated dissociation channel contribution.

7.4 Summary and Conclusions

In this study we employed the AIMD method to determine the sticking probability for N_2 on W(110). Our method includes improvements with respect to a previous static surface study since we explicitly model surface temperature and surface motion effects. The AIMD results, obtained with two different GGA density functionals (PBE and RPBE), are considerably different from the previous static-surface results, especially for the trapping-mediated dissociation channel, which dominates at low energies. The presence of deep adsorption minima in the multidimensional PES sampled by AIMD, together with a significant energy transfer to the surface, are suggested to be responsible

for the large indirect dissociation probability: molecules that are molecularly adsorbed often dissipate kinetic energy to phonons such that they no longer find their way back to the gas phase, with dissociation or molecular adsorption as only possible outcomes. Agreement with experiments is reasonable at high energies, but the AIMD method fails to reproduce the experimental trend according to which the dissociation probability increases with collision energy, predicting a probability that is insensitive to E_i. At low energies, AIMD overestimates the experimental dissociation probability. We attribute the mismatch between the AIMD results and experiments to a failure of both the PBE and RPBE functionals to reproduce the experimental molecular adsorption energies, and the fact that the RPBE functional returns lower molecular adsorption energies might explain the better agreement obtained with this functional with experiments for the dissociation probability at low collision energy.

7.A Appendix

7.A.1 NEB Calculations

In the following Figures we present the results of the CI-NEB calculations. Four images (labeled as 1-4) have been optimized between each of the molecular adsorption configurations (reactants, R) and the lowest-energy dissociated adsorption state (products, P). The zero of energy is defined as the energy of the molecule in its equilibrium geometry placed midway between two slabs.

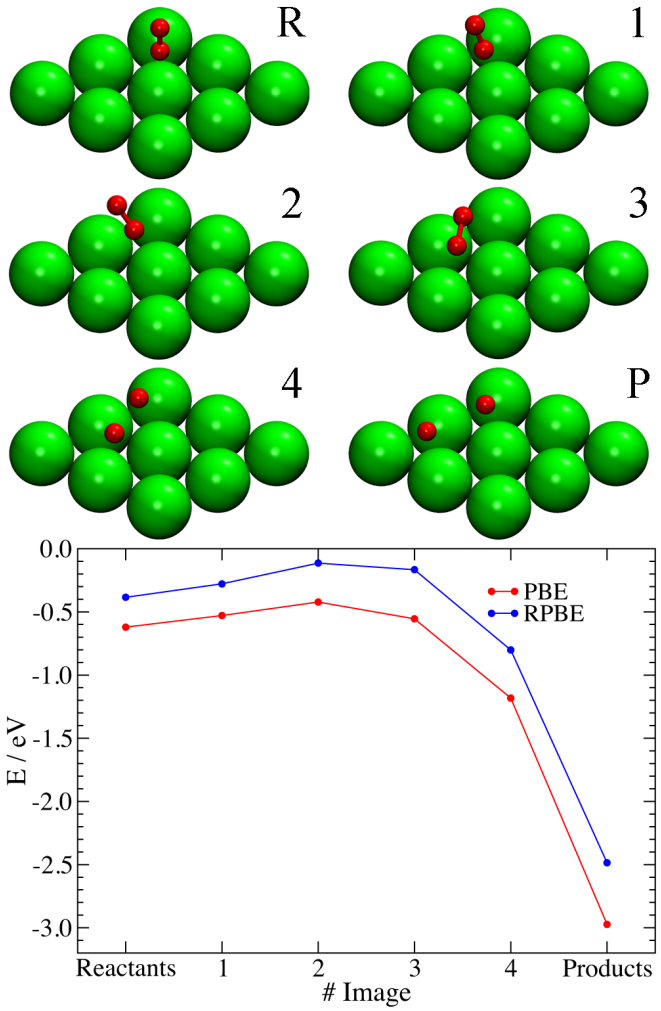

Figure 7.A.1: Results of CI-NEB calculations in which the reactants correspond to the top-vertical molecular adsorption geometry. In the lower panel, the energy of each configuration is plotted as a function of the image number. Red is for PBE and blue for RPBE. Straight lines connect points corresponding to consecutive images. The molecular configurations, as well as first layer surface atoms, are schematically represented above.

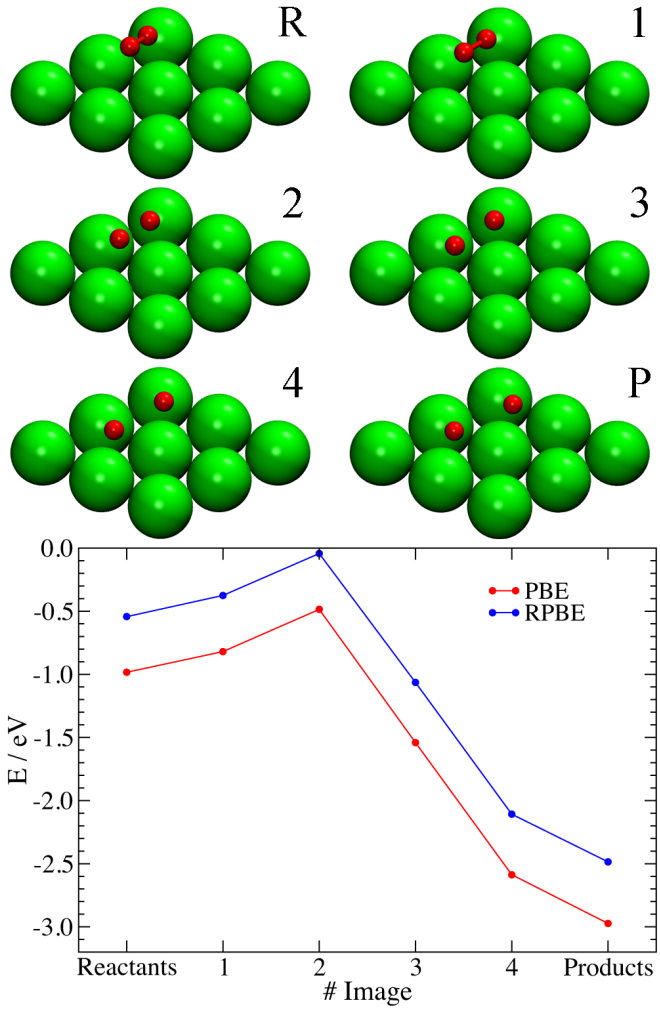

Figure 7.A.2: Same as Figure 7.A.1, but the reactants correspond here to the bridge/hollow-tilted molecular adsorption configuration.

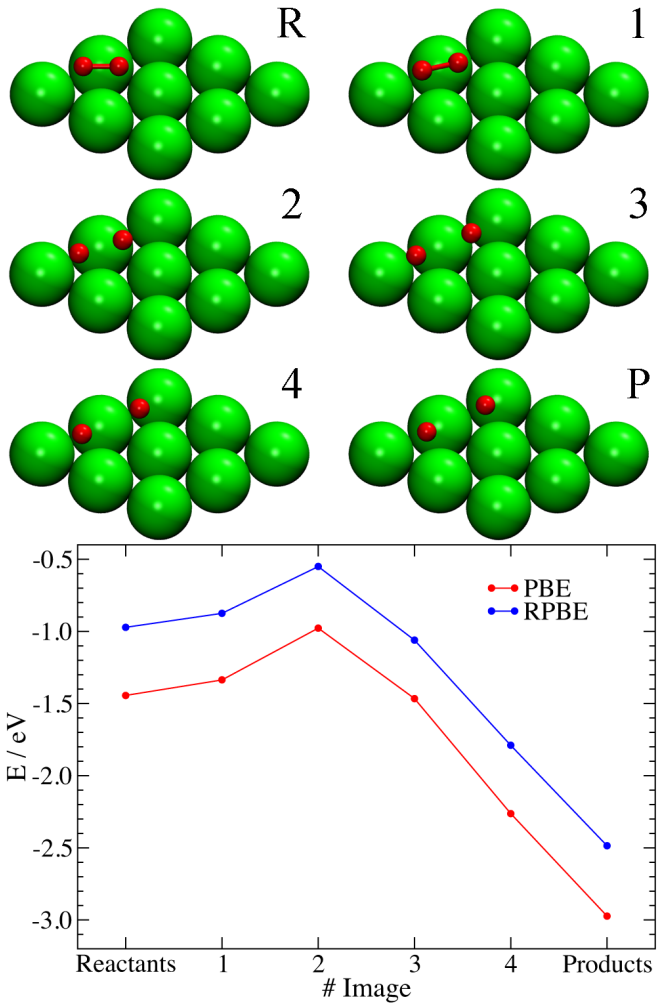

Figure 7.A.3: Same as Figure 7.A.1, but the reactants correspond here to the hollow-parallel molecular adsorption configuration.

Bibliography

[1] G. Ertl, Catal. Rev. Sci. Eng. **21**, 201 (1980).

[2] S. P. Singh-Boparai, M. Bowker, and D. A. King, Surf. Sci. **53**, 55 (1975).

[3] J. T. Yates, R. Klein, and T. E. Madey, Surf. Sci. **58**, 469 (1976).

[4] R. C. Cosser, S. R. Bare, S. M. Francis, and D. A. King, Vacuum **31**, 503 (1981).

[5] H. E. Pfnür, C. T. Rettner, J. Lee, R. J. Madix, and D. J. Auerbach, J. Chem. Phys. **85**, 7452 (1986).

[6] A. Kara and A. E. DePristo, J. Chem. Phys. **88**, 2033 (1988).

[7] J. C. Lin, N. Shamir, Y. B. Zhao, and R. Gomer, Surf. Sci. **231**, 333 (1990).

[8] Q. J. Zhang, J. C. Lin, N. Shamir, and R. Gomer, Surf. Sci. **231**, 344 (1990).

[9] C. T. Rettner, E. K. Schweizer, and H. Stein, J. Chem. Phys. **93**, 1442 (1990).

[10] T. F. Hanisco and A. C. Kummel, J. Vac. Sci. Technol. A **11**, 1907 (1993).

[11] G. Volpilhac and A. Salin, Surf. Sci. **556**, 129 (2004).

[12] M. Alducin, R. Díez Muiño, H. F. Busnengo, and A. Salin, J. Chem. Phys. **125**, 144705 (2006).

[13] M. Alducin, R. Díez Muiño, H. F. Busnengo, and A. Salin, Phys. Rev. Lett. **97**, 056102 (2006).

[14] M. Alducin, R. Díez Muiño, H. F. Busnengo, and A. Salin, Surf. Sci. **601**, 3726 (2007).

[15] G. A. Bocan, R. Díez Muiño, M. Alducin, H. F. Busnengo, and A. Salin, J. Chem. Phys. **128**, 154704 (2008).

[16] J. I. Juaristi, M. Alducin, R. Díez Muiño, H. F. Busnengo, and A. Salin, Phys. Rev. Lett. **100**, 116102 (2008).

[17] S. Riikonen, A. S. Foster, A. V. Krasheninnikov, and R. M. Nieminen, Phys. Rev. B **80**, 155429 (2009).

[18] I. Goikoetxea, J. I. Juaristi, M. Alducin, and R. Díez Muiño, J. Phys.: Condens. Matter **21**, 264007 (2009).

[19] K. R. Geethalakshmi, J. I. Juaristi, R. Díez Muiño, and M. Alducin, Phys. Chem. Chem. Phys. **13**, 4357 (2011).

[20] L. Martin-Gondre, M. Alducin, G. A. Bocan, R. Díez Muiño, and J. I. Juaristi, Phys. Rev. Lett. **108**, 096101 (2012).

[21] R. Pétuya, P. A. Plötz, C. Crespos, and P. Larregaray, J. Phys. Chem. C **118**, 21904 (2014).

[22] J. P. Perdew, J. A. Chevary, S. H. Vosko, K. A. Jackson, M. R. Pederson, D. J. Singh, and C. Fiolhais, Phys. Rev. B **46**, 6671 (1992).

[23] J. P. Perdew, J. A. Chevary, S. H. Vosko, K. A. Jackson, M. R. Pederson, D. J. Singh, and C. Fiolhais, Phys. Rev. B **48**, 4978 (1993).

[24] B. Hammer, L. B. Hansen, and J. K. Nørskov, Phys. Rev. B **59**, 7413 (1999).

[25] G. J. Kroes, Science **321**, 794 (2008).

[26] A. C. Luntz, I. Makkonen, M. Persson, S. Holloway, D. M. Bird, and M. S. Mizielinski, Phys. Rev. Lett. **102**, 109601 (2009).

[27] J. I. Juaristi, M. Alducin, R. Díez Muiño, H. F. Busnengo, and A. Salin, Phys. Rev. Lett. **102**, 109602 (2009).

[28] G. J. Kroes, Phys. Chem. Chem. Phys. **14**, 14966 (2012).

[29] L. Martin-Gondre, J. I. Juaristi, M. Blanco-Rey, R. Díez Muiño, and M. Alducin, J. Chem. Phys. **142**, 074704 (2015).

[30] M. Dion, H. Rydberg, E. Schröder, D. C. Langreth, and B. I. Lundqvist, Phys. Rev. Lett. **92**, 246401 (2004).

[31] K. Lee, E. D. Murray, L. Kong, B. I. Lundqvist, and D. C. Langreth, Phys. Rev. B **82**, 081101 (2010).

[32] A. De Vita, I. Štich, M. J. Gillan, M. C. Payne, and L. J. Clarke, Phys. Rev. Lett. **71**, 1276 (1993).

[33] I. Štich, M. C. Payne, A. De Vita, M. J. Gillan, and L. J. Clarke, Chem. Phys. Lett. **212**, 617 (1993).

[34] I. Štich, A. De Vita, M. C. Payne, M. J. Gillan, and L. J. Clarke, Phys. Rev. B **49**, 8076 (1994).

[35] A. Groß and A. Dianat, Phys. Rev. Lett. **98**, 206107 (2007).

[36] F. Nattino, C. Díaz, B. Jackson, and G. J. Kroes, Phys. Rev. Lett. **108**, 236104 (2012).

[37] F. Nattino, H. Ueta, H. Chadwick, M. E. van Reijzen, R. D. Beck, B. Jackson, M. C. van Hemert, and G. J. Kroes, J. Phys. Chem. Lett. **5**, 1294 (2014).

[38] L. S. Dubrovinsky and S. K. Saxena, Phys. Chem. Miner. **24**, 547 (1997).

[39] J. S. Shah and M. E. Straumanis, J. Appl. Phys. **42**, 3288 (1971).

[40] V. F. Sears and S. A. Shelley, Acta Crystallogr., Sect. A **47**, 441 (1991).

[41] J. C. Buchholz, G. C. Wang, and M. G. Lagally, Surf. Sci. **49**, 508 (1975).

[42] R. J. Smith, C. Hennessy, M. W. Kim, C. N. Whang, M. Worthington, and M. D. Xu, Phys. Rev. Lett. **58**, 702 (1987).

[43] G. Kresse and J. Hafner, Phys. Rev. B **47**, 558 (1993).

[44] G. Kresse and J. Hafner, Phys. Rev. B **49**, 14251 (1994).

[45] G. Kresse and J. Furthmüller, Comput. Mat. Sci. **6**, 15 (1996).

[46] G. Kresse and J. Furthmüller, Phys. Rev. B **54**, 11169 (1996).

[47] G. Kresse and D. Joubert, Phys. Rev. B **59**, 1758 (1999).

[48] P. E. Blöchl, Phys. Rev. B **50**, 17953 (1994).

[49] J. P. Perdew, K. Burke, and M. Ernzerhof, Phys. Rev. Lett. **77**, 3865 (1996).

[50] J. P. Perdew, K. Burke, and M. Ernzerhof, Phys. Rev. Lett. **78**, 1396 (1997).

[51] W. L. Hayes, *Statistics*, Holt, Rinehart and Winston, NY, 3rd edition, 1981.

[52] V. Blum, R. Gehrke, F. Hanke, P. Havu, V. Havu, X. Ren, K. Reuter, and M. Scheffler, Comput. Phys. Commun. **180**, 2175 (2009).

[53] G. Henkelman, B. P. Uberuaga, and H. Jónsson, J. Chem. Phys. **113**, 9901 (2000).

[54] G. Henkelman and H. Jónsson, J. Chem. Phys. **113**, 9978 (2000).

[55] E. Bitzek, P. Koskinen, F. Gähler, M. Moseler, and P. Gumbsch, Phys. Rev. Lett. **97**, 170201 (2006).

[56] I. Goikoetxea, M. Alducin, R. Díez Muiño, and J. I. Juaristi, Phys. Chem. Chem. Phys. **14**, 7471 (2012).

[57] I. Goikoetxea, J. I. Juaristi, R. Díez Muiño, and M. Alducin, Phys. Rev. Lett. **113**, 066103 (2014).

[58] M. Alducin, Private Communication, 2015.

[59] T. A. Delchar and G. Ehrlich, J. Chem. Phys. **42**, 2686 (1965).

[60] B. Baule, Ann. Physik. **44**, 145 (1914).

[61] A. Gross, *Theoretical Surface Science*, Springer, Berlin, 2003.

[62] F. O. Goodman, J. Phys. Chem. **84**, 1431 (1980).

[63] S. H. P. Chen and S. C. Saxena, Int. J. Heat Mass Transfer **17**, 185 (1974).

[64] S. C. Saxena and S. H. P. Chen, J. Phys. B: At. Mol. Phys. **10**, 2011 (1977).